PHYSICAL REVIEW B VOLUME 56, NUMBER 18 1 NOVEMBER 1997-II

Magneto-optical studies of magnetization of melt-processed $YBa_2Cu_3O_{7-\delta}$

L. S. Uspenskaya, V. K. Vlasko-Vlasov, and V. I. Nikitenko
Institute of Solid State Physics RASc, 142432 Chernogolovka, Moscow district, Russia

T. H. Johansen
University of Oslo, P.O. Box 1048, Blindern, N-0316 Oslo, Norway

(Received 21 March 1997)

Magnetization patterns on different faces of long bars cut from melt-processed $YBa_2Cu_3O_{7-\delta}$ (YBCO) samples were studied using advanced magneto-optical techniques. It is shown that with an external magnetic field perpendicular to the long side of the bar the magnetization front is described by a cylindrical surface having a cross section shaped as a higher-order ellipse, i.e., the front has a sharper bending near the sample edges than a second-order ellipse. Similar to bicrystal boundaries, the boundaries of structure domains consisting of c axis-aligned crystalline plates are revealed to be weak links in a wide temperature range for misorientation angles between domains exceeding 10°. The temperature dependence of the critical currents inside the domains are determined by fitting induction profiles measured across the bars. From direct flux pattern observations and measurements of the anisotropy for currents flowing along and across the crystalline plates, it follows that the crystallite boundaries also become effective weak links at higher temperatures and fields. Possible reasons for why the observed anisotropy is much less than that for c axis and ab plane currents in YBCO single crystals are discussed. [S0163-1829(97)00938-7]

INTRODUCTION

Melt-processed $YBa_2Cu_3O_{7-\delta}$ (MP YBCO) (Refs. 1 and 2) is today the most advantageous high-temperature superconductor (HTSC) for many bulk applications like magnetic suspensions, bearings, rotors, and so on. These materials possess the highest critical current, $J_c \sim 10^5$ A/cm^2, at liquid-nitrogen temperature (yielding only to YBCO films), a moderate decrease of J_c in external fields, and large areas—so-called structure domains—free of weak links. This allows trapping of large magnetic moments, which is important for many superconducting devices. So far it is not fully understood what is the mechanism of enhanced J_c in MP YBCO although 211 inclusions,[3] interfaces between 211 and 123 phases,[4] twin boundaries,[5] or dislocations[6] and stacking faults[7] generated around 211 particles have been proposed as important pinning centers. It is generally recognized, however, that the alignment of crystal plates (crystallites) having a common c axis within structure domains is the main reason for a reduced number of weak links in the material. Weak links are usually associated with grain boundaries and limit the current-carrying ability of the ceramical HTSC's. In MP samples the boundaries between crystallites in the structure domains have small misorientation angles, but in some parts cracks and precipitates of nonsuperconducting phases can form during the growth process.[2,8] Nevertheless, these boundaries are considered to provide good contact between crystallites due to the existence of well-coupling bridges. Much worse are the superconducting properties at boundaries *between* structure domains, which in general have large misorientation of c axes. Peculiarities of the magnetic-flux behavior due to both types of boundaries are directly studied in the present paper using magneto-optical observations.

The problem of grain boundaries (note that in low-T_c superconductors the grain boundaries are one of the main factors for improving pinning and thus J_c.) in cuprates has been discussed intensively since the discovery of HTSC's.[9] It was clarified that their structure depends on fine changes in the composition as well as conditions of sample preparation and processing. In turn, the superconducting properties of grain boundaries should be extremely sensitive to details of their structure due to the very short coherence length in the HTSC's. This results in different effects of the grain boundaries in differently grown samples, and therefore requires a detailed study in a specific material. At present the most consistent investigations of the effects of grain boundaries are performed on artificial film structures grown on bicrystal substrates, see Refs. 9–11, which show deterioration of the superconducting properties at boundaries with misorientation angles above $\sim 10°$. There are also several works on intergrown single crystal[12–14] confirming pinning effects at low-angle grain boundaries and weak-link behavior at high angles (excluding special orientations). However, only a few papers focus on this problem in melt-processed HTSC's (Refs. 15–17), where mostly the magnetic properties of samples cut from separate structure domains have been reported. An anisotropy of critical currents along and perpendicular to aligned crystallites was observed at 77 (Ref. 15) and 5 K (Ref. 16), and turned out to be less than that for the same directions in single crystals of YBCO. It was also shown that inside domains[2] the temperature and magnetic-field dependences of J_c are improved, especially at lower fields and higher temperatures, by increasing the content of 211 inclusions, thus indicating their dominant role in bulk pinning. As for the domain boundaries their effects were studied much less. It is only known that due to the structure imperfection of large angle boundaries[18,19] they should produce weak links. This was confirmed recently by magneto-optical experiments.[20]

In MP HTSC's there are usually several domains having

0163-1829/97/56(18)/11979(10)/$10.00

different c-axis orientations so that in a bulk sample the crystallites are aligned at different angles to the sample faces. This should result in inhomogeneous flux and current distributions determined not only by the value and anisotropy of the critical current in domains, but also by the arrangement of domains relative to the field and the sample edges. The main goal of the present work was to analyze magnetic-flux and current patterns in MP samples containing several domains using real-time high-resolution magneto-optical techniques, in order to clarify the role of domain and crystallite boundaries in the magnetic response of the material at different temperatures. At the same time, effects of the sample shape on the magnetization front geometry were studied. Our observations directly reveal peculiarities in the behavior of bulk MP HTSC's in superconducting devices.

EXPERIMENT

Long rectangular bars ($\sim 0.4 \times 1 \times 10$ mm) were cut from bulk MP YBCO samples containing several structure domains. In the domains crystalline plates are known to be aligned with a common c axis and with ab axes only slightly (of the order of a few degrees) rotated in neighboring crystallites.[2,18–19] To determine orientations of the axes in different domains, samples were polished and the directions of cracks along crystallite boundaries and directions of twins on mutually perpendicular faces were examined in a polarizing microscope. Figures 1(a) and 1(b) show low magnification images of domains on two faces of one sample. The contrast in domains is determined by the bireflectance giving different colors for different orientations of crystal axes with respect to the polarization of the incident light. The same contrast also appears between the different twins, seen at the larger magnification in Fig. 1(c). In Fig. 1(c) one can also see lines of cracks along the projections of basal planes of crystallites in domains on the sample faces as well as 211 inclusions of relatively large dimensions. Cracks are interrupted and bridges between the crystallites are clearly observed. This is a typical picture for MP YBCO. It is known from literature, e.g., Refs. 18, 21, and 22, that at boundaries between the domains, and also between crystallites, there can be Cu and Ba oxides, some amorphous phases, microcracks, and oxygen depletion. Electron microscopic observations reveal precipitates and twin structures down to nanometers,[2,18,19] and also numerous dislocations and stacking faults in 211/123 interface regions.[5–7] Figure 1(d) gives a schematic drawing of the orientations of crystal plates and c axes in the domains of the present sample retrieved from twin and crystallite boundary directions on different faces. Note that in domain 1 the crystallites are oriented normal to the long edges of the sample bar. In domain 2 the orientation is parallel, while in domain 3 the crystallites are inclined at some angle.

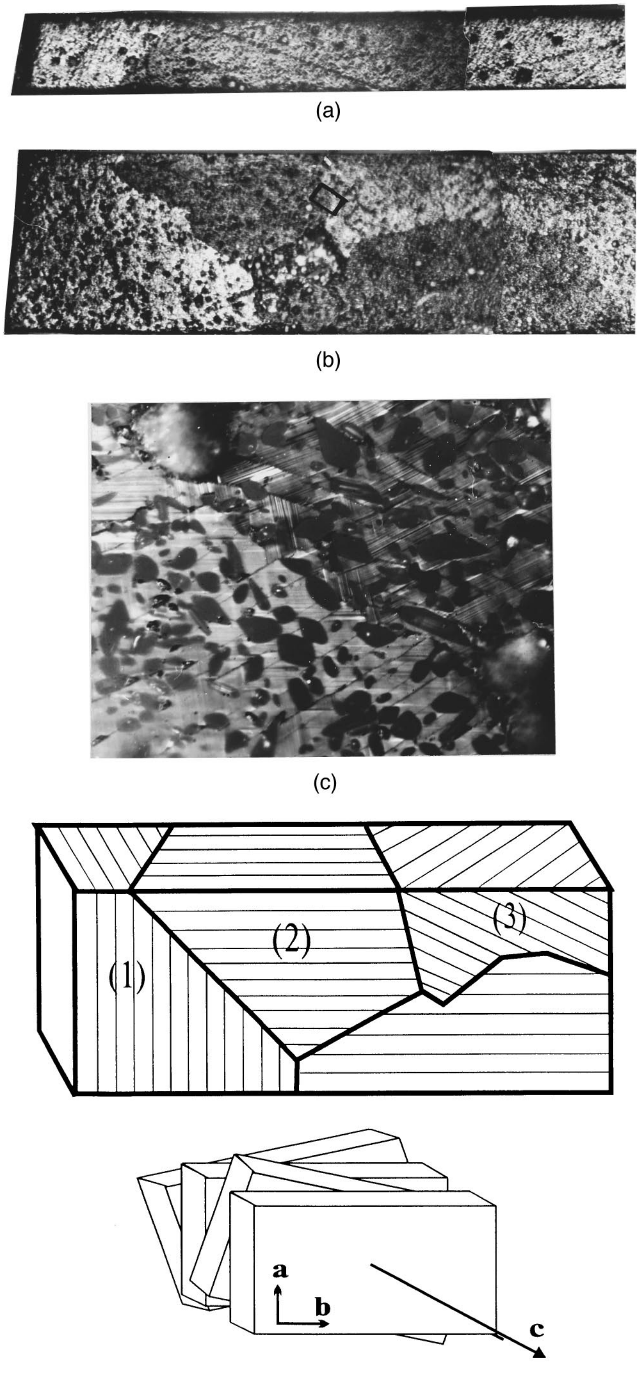
(a)

(b)

(c)

(d)

FIG. 1. (a,b) Polarized light image of structure domains on two faces of a rectangular bar of a melt-processed YBCO. (c) Magnification of the area marked by a box in (b). Darker spots of 211 particles, parallel stripes of twin structures, and cracks along boundaries of some crystallites are visible in the domains. (d) Schematics of the orientation of crystal platelets and their c axes in the domains of the sample under study.

Samples were glued to the cold finger of an optical cryostat and one face was covered with a sensitive iron garnet film with the in-plane anisotropy. Such a magneto-optical indicator can reveal in a polarizing microscope real-time variations of the normal component of induction B_n on the sample surface with practically an optical resolution in a wide temperature range.[23] In the pictures below the image brightness corresponds to the local-field value observed in the indicator plane with the external field applied normal to the sample face. To quantify the local field a modulation technique was used which provided measurements of the Faraday angle α in regions $\sim 3\ \mu$m in diameter. By scanning the Faraday angle measurement along chosen tracks, and using a calibration curve $\alpha(B_n)$ for the film, we could obtain

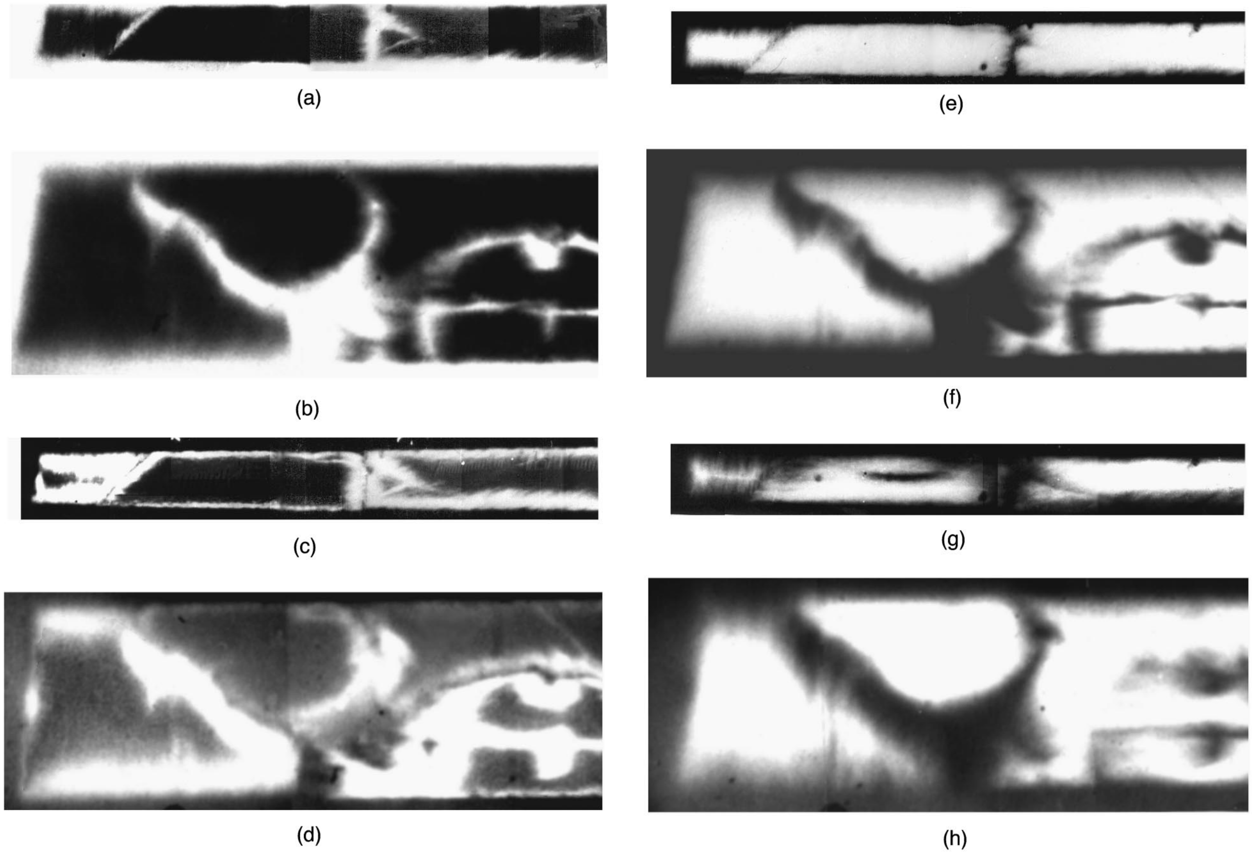

FIG. 2. Magneto-optic images of penetration and trapping of magnetic flux in external fields normal to the wide and narrow side of the sample shown in Fig. 1. The polarizers were nearly uncrossed, and color brightness represents the local-field magnitude. In (a) and (b) $H_a=935$ Oe. In (c) and (d) $H_a=0$ after first applying 1170 Oe (e) and (f) show the trapped flux after field cooling in 1170 Oe down to $T=16$ K. (g) and (h) show the same after cooling down to 70 K.

profiles of $B_n(x)$ in different domains. These profiles were numerically fitted by calculated induction profiles on the surface of a bar with the same length and with the same cross section (perpendicular to the long side of the sample) as the sample. The critical current J_c was assumed to flow parallel to the long edge in a shell; near the surface at smaller fields, and across the whole bar cross section at total flux penetration. Currents have opposite signs in two halves of the sample. This picture corresponds to the Bean model for the field entry with a front separating the inner Meissner state from the outer shell filled with vortices. The front shape was selected as a cylindrical surface with a cross section given by some even order curve (details described below). In this way the qualitative features of measured B_n profiles were reproduced. The characteristic dimensions of the curve together with the magnitude of J_c were used as fitting parameters. From these fits we were able to determine the critical current density and its temperature dependence for different domains.

RESULTS

Features of the field penetration

Figure 2 illustrates the flux entry and subsequent trapping in the sample shown in Fig. 1. The set of pictures was taken with the field applied normal to the bar's wide and narrow surface, respectively. One observes that the field starts penetrating in the boundaries between structure domains [Figs. 2(a) and 2(b)], and that it also escapes first from the same regions at decreasing field; see the darker lines along the boundaries in Figs. 2(c) and 2(d) which show a reduced and reversed field there. In this case the angles between c axes in different domains exceed 20° and all the boundaries definitely show the weak-link behavior. It should be noted, however, that no weak-link effects were observed at domain boundaries with angles below $\sim 10°$ (not shown in Fig. 2) in fields up to 1.5 kOe. The same observation was reported also in Ref. 20. By direct inspection we found cracks and precipitates of other phases along the large-angle domain boundaries. However, there were also long segments where no such defects showed up within the optical resolution. Therefore, the observed weak-link behavior can be attributed to intrinsic properties of these boundaries, which is consistent with data for bicrystal boundaries in epitaxial YBCO structures.[10]

By increasing the applied field further the screening currents start to form closed loops inside each domain, i.e., they follow the shape of the domains, and the flux enters inside both from the sample surface as well as from the domain boundaries. In a sense, in the high-field magnetization process the domain boundaries behave effectively as additional surface area of the sample. Distinct easy penetration directions are seen to lie in the *ab* plane. In Fig. 2 this effect becomes most evident by comparing the flux patterns in domains 1 and 2 where crystallites are oriented perpendicular and parallel to the bar length, respectively.

The easier field penetration along the basal plane was previously observed in single-domain samples of melt-processed YBCO at 10 and 77 K (Ref. 15) by Goto *et al.*, and also later at 5 K by Schuster *et al.*[16] The ratio of critical currents flowing along and perpendicular to the basal plane estimated from the penetration depth in different directions was 3 at 77 K in Ref. 15 and 25 at 5 K in Ref. 16. These ratios were smaller than expected for single crystals of YBCO. We have measured this anisotropy in a wide temperature range as discussed below.

At higher magnifications bright spots are visible inside domains. They appear due to the flow of screening currents around large 211 particles and show wiggling trajectories of J_c in the material (not shown in the picture). One more source of the pattern irregularity is the crystallite boundaries in domains. They result in a furlike front of the flux entry in domains with ''hairs'' along the crystal platelets. This was observed also in Ref. 16 but considered as a picture similar to the penetration front in crystals. We emphasize the special structure of this front showing zigzag trajectories of supercurrents due to cracks and perhaps also weak links along the crystallite boundaries. This peculiarity results in a difference of magnetization processes in MP samples as compared to single crystals, e.g., it suppresses formation of Meissner holes[24] and macroturbulent structures[25,26] which are observed in remagnetized YBCO crystals. Nevertheless, for the estimation one may treat the present flux patterns in terms of an average J_c flowing at an appropriate angle to the crystallites, neglecting that the actual current trajectories are wiggling.

After turning on and switching off the applied field the width of bright rim representing trapped flux [Figs. 2(c) and 2(d)] directly shows the ratio of critical currents flowing in different domains along their boundaries. If the sample is cooled in a field which is subsequently switched off at low temperature the flux will escape from the boundary regions in accordance with the appropriate critical currents in the domains. In this case the flux of opposite polarity due to the return field of the trapped flux enters along the boundaries and near the sample edges [Figs. 2(e) and 2(f)].

At higher temperatures the penetration fields become essentially smaller and the anisotropy increases. However, the qualitative features of the magnetization processes remain the same, as can be seen by comparing Figs. 2(e) and 2(f) at 16 K and Figs. 2(g) and 2(h) taken at 70 K.

Field profiles

Field profiles measured across the sample during penetration and trapping of magnetic flux in domains are shown in Figs. 3 and 4. The set of profiles in Fig. 3 are measured on the narrow face of the bar in domain 2 after application of fields starting from 200 Oe and increasing in steps of 100 Oe at 15 K. Figure 4 shows the same field scan after the sample was initially cooled to 15 K in various applied fields, which subsequently were switched off. The same sets of profiles obtained for domain 1 are shown in Figs. 5 and 6. While the general changes of the profiles are the same in both domains, it is evident that flux penetrates more easily into domain 1 than into domain 2 at equal applied fields. The difference in the slope of the field profiles shows that J_c of domain 2 is higher. Figure 7 illustrates how increasing the temperature tends to flatten the trapped flux profiles in domain 2. This is due to a monotonically decreasing $J_c(T)$.

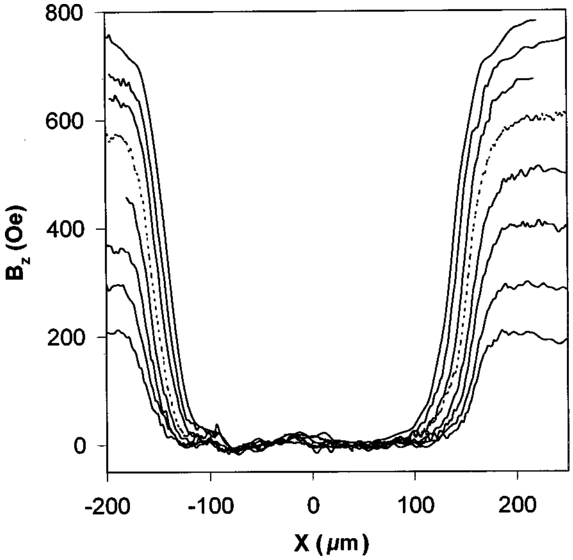

FIG. 3. Perpendicular induction profiles measured across the zfc sample in domain 2 at 15 K. The lowest curve was obtained with $H_a = 200$ Oe, and for each next curve H_a was increased by 100 Oe.

To model the observed flux profiles consider first the simple case of a plate in a parallel field assuming that the flux penetration front is parallel to the faces, see Fig. 8. Numerical calculations of $B_n(x)$ for current sheets of increasing thickness and of constant current density are shown. In the calculations, which are based on the Biot-Savart law, the rectangular cross section of the bar was set equal to that of the sample and the field was evaluated in a plane 5 μm above the upper bar face corresponding to the plane of the

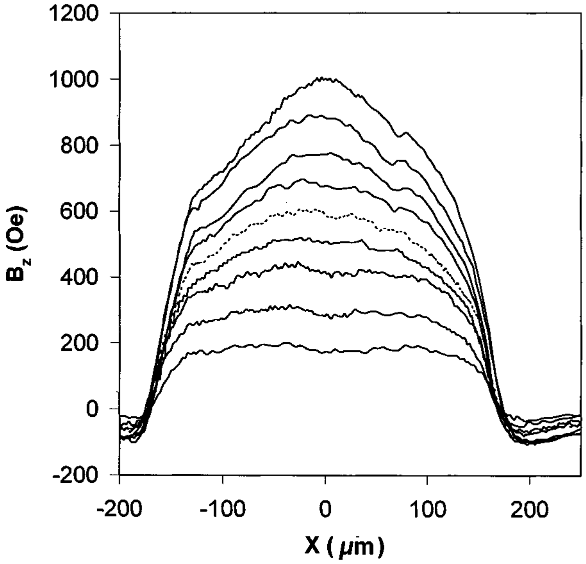

FIG. 4. Profiles of the trapped flux ($H_a = 0$) in domain 2 after cooling to 15 K in fields from 200 (lower) to 1000 (upper) Oe with steps of 100 Oe.

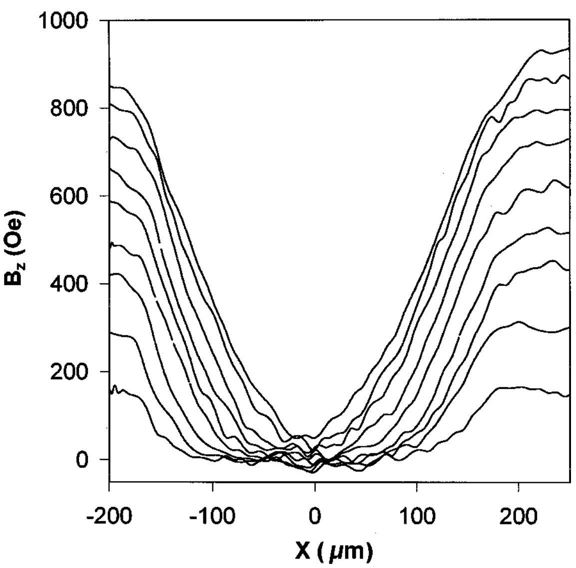

FIG. 5. Flux penetration in domain 1 for the same conditions as in Fig. 3.

indicator film. The edges of the rectangle were rounded with a radius of curvature of $\sim 8\ \mu$m, simulating the sample shape after polishing.

A qualitative discrepancy between calculated and measured profiles is seen at their wings outside the sample edges. Here the experimental $B_n(x)$ displays a maximum near the edge at the smaller fields (Fig. 3). In larger fields this peak vanishes, and the flux profile becomes monotonically increasing towards a level given by the applied field. The observed field concentration near the edges is caused by currents flowing in the corners where the initial flux penetration takes place. One possible reason for the change in the profile shape could be a suppression of J_c in the corners (e.g., as discussed in Ref. 27) by the enhanced external field. However, there is also the possibility that the effect is related to the displacement of the magnetization front. To clarify this we modeled the penetration front by a cylindrical surface with a cross section given by

$$(x/a)^{2n}+(y/b)^{2n}=1. \tag{1}$$

By using different powers n this describes various ''ellipsoids'' inscribed into a rectangle with sides a and b. At larger powers the front will bend more sharply in the corners, as illustrated in Fig. 9. With increasing applied field the flux front was assumed to shift inwards from the sides but not from the top and bottom. Thus, the penetration front is deformed only by a shortening of the a axis of the ellipsoid. In the calculations the shell carrying J_c was divided into square filaments with $\Delta x \times \Delta z \sim 0.85 \times 0.85\ \mu\text{m}^2$. To allow a more

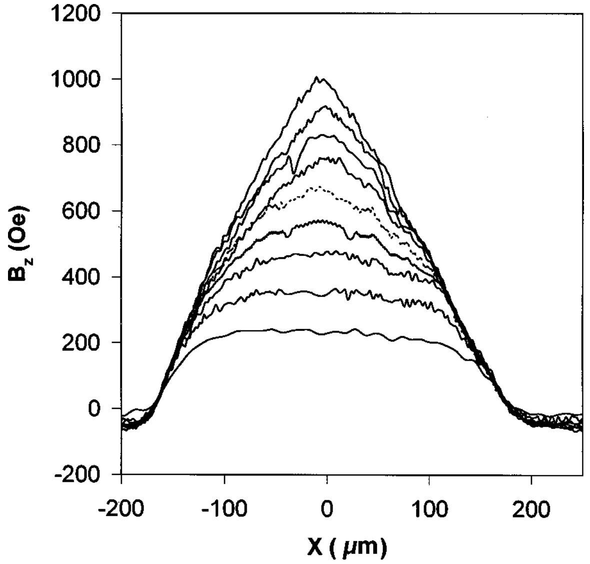

FIG. 6. Profiles of trapped flux in domain 1 for the same conditions as in Fig. 4.

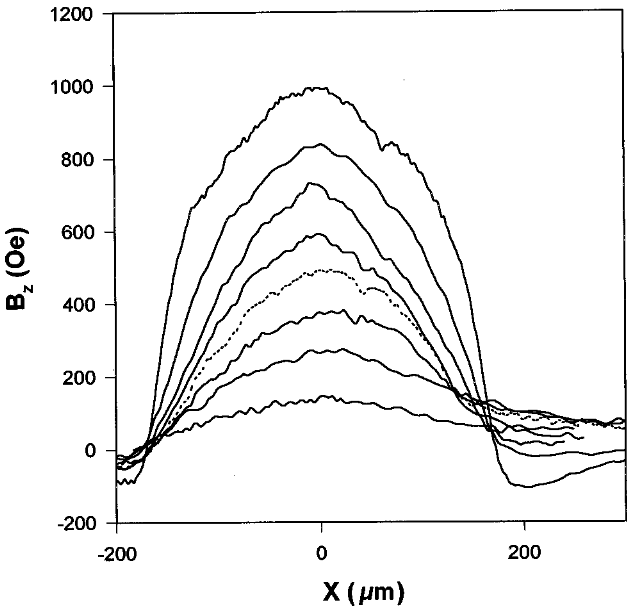

FIG. 7. Temperature changes of the trapped flux profile in domain 2 after field cooling in $H_a = 1$ kOe. The curves were obtained for $T = 11$, 40, 63, 69, 76, 79, 82, 85, 87, and 88.5 K.

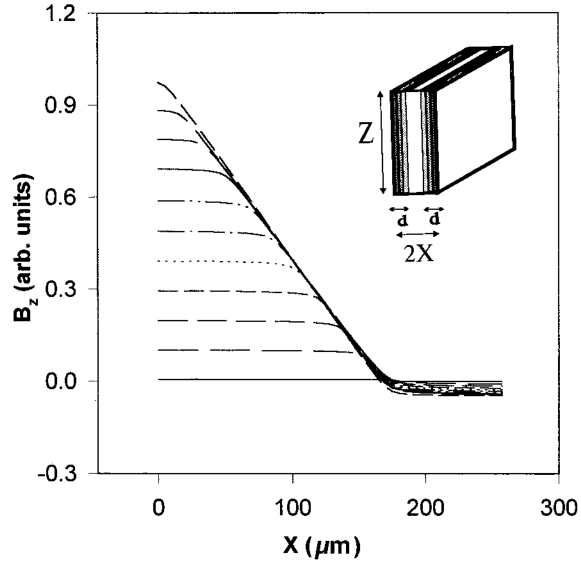

FIG. 8. Calculated $B_n(x)$ on the top face of an infinitely long rectangular bar with currents flowing along the sides as shown in the insert. The graphs illustrate how the profiles develop with increasing thickness d of the current carrying layer.

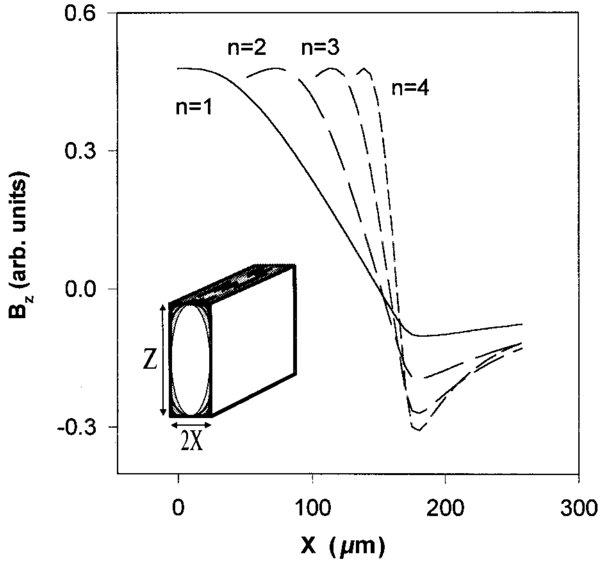

FIG. 9. Profiles of $B_n(x)$ on the top surface of an infinitely long rectangular bar carrying currents in the shell limited by the bar faces and different cylindrical surfaces with cross section $(x/a)^{2n}+(y/b)^{2n}=1$, i.e., an ''ellipsoid'' of order n. Curves are shown for $n=1$, 2, 3, and 4 where calculations were made for flux penetration depths $d=0$. The slight dip in the profiles near the center is due to the spatial discretization made in the calculations. The current was set equal to zero in filaments close to the face center, where the current carrying layer is less than Δz_1 in thickness. The inset illustrates how ellipsoids of different order vary in shape.

detailed description of the surface layer the filaments at the top and bottom were chosen with $\Delta x_1=\Delta x$ and $\Delta z_1=0.1\,\Delta z$.

There is initially a peak in $B_n(x)$ near the sample edges for all powers n. The squeezing of the short ellipsoid axis, which also implies a displacement of the strongly bent part of the penetration front away from the rectangle corners, reduces the peak. Eventually the peak vanishes completely.

Comparison with the experimental profiles of Fig. 3 shows that the ellipsoid of the second order ($n=1$) is not a good description of the penetration front. The predicted profiles $B_n(x)$ for $n=1$ clearly lack the abrupt change from the flat central part to the steep slopes of the U-shaped profiles observed experimentally. By increasing the power the calculated profiles attain the characteristic ''bucket'' shape first at $n=3$, where also the nearly linear drop of B_n near the sample edges is reproduced. Thus we conclude that the flux penetration front in rectangular bars has initially a shape which is strongly bending near the corners. This is in accordance with a recent calculation, due to Brandt, on the electrodynamical problem for magnetization of long rectangular bars in transverse fields.[28] The induction lines in Fig. 1 of Ref. 29 just show stronger bending in the corners of the rectangles at the initial stages of magnetization. The bending becomes smooth only at fields about half of the total penetration field. Note that during the displacement of the penetration front the positive field above the sample in Fig. 9 (we remind the reader that this is only the field due to J_c which should be added to the external field H_{ext}) is increasing much stronger than the negative one decreases outside and their ratio becomes larger. This helps to make initial estimates of fitting parameters from the comparison of field values in the middle and at the wings of measured profiles.

Our numerical calculations showed that the field profile $B_n(x)$ at the sample surface is not very sensitive to slight changes in the shape of the magnetization front. In fact, if the sixth-order ellipsoid is substituted by an appropriate polygon circumscribing the ellipsoid, the resulting $B_n(x)$ is practically the same. This was used to simplify the estimation of J_c from the profiles measured at moderate fields. Moreover, the calculations show that the profile shape is nearly insensitive to the currents flowing far from the top surface. Therefore, symmetrical magnetization fronts were assumed in the fits for each domain, even when they did not extend throughout the entire sample thickness.

We also notice that if a field H_a is applied to a zero-field-cooled (zfc) sample and then switched off, the remnant flux profile will have a maximum noticeably less than the naively expected $H_a/2$. Therefore, in this remnant state the profile has a smaller slope than in the trapped flux state produced by field cooling. In the first case the flux initially enters the sample with an ''elliptic'' front, which at large applied fields will go to the very center. The flux exit process then leads to a second elliptic front. Between the ellipses a positive J_c flows and between the outer ellipse and the sample surface the current has the opposite sign. Superimposing the field from $+J_c$ and $-J_c$ in layers of different effective thickness the result is a reduced slope of $B_n(x)$.

Our results (Figs. 3–6) show that the profiles of flux trapped after field cooling have features different from those obtained by application of the same fields to the zfc bar. If J_c were only a function of temperature, and one neglects a Meissner current contribution (not seen in the experiment), one should expect in the fc case that after setting $H_a=0$, a flux gradient will be present in the same regions as those invaded by flux in the virgin state when the same field is applied. Thus, profiles of trapped flux should coincide with the inverted penetration profiles. This is in fact observed at small fields. At larger fields, however, only the slope near the edges is the same for the fc and zfc profiles. Differences are seen in the central parts and also in the profile wings outside the sample edges. First of all, instead of the plateau observed in the zfc case there is a slope in the central region which increases with H_a for the fc sample. It is smaller than the slope near the edges and corresponds to smaller currents flowing in the interior as compared to a larger J_c near the edge. The finite slope in the middle of the fc profiles is associated with a deeper location of the flux exit front, i.e., an expansion of the current-carrying shell as compared to the zfc case, and also a field suppression of the magnitude of J_c in the central region. During virgin magnetization of the zfc sample the flux front enters less deeply and J_c is suppressed only near the corners. By increasing the field in which the sample is cooled the current-carrying shell formed by setting $H_a=0$ will expand inside the bar, and a peak in $B_n(x)$ above the sample should become sharper in spite of the effect of a field-dependent J_c. This explains the increasing steepness of the fc profiles in the center of the bar at larger H_a in Figs. 4 and 6.

As discussed above, the observed wings of the zfc profiles outside the sample edges change from being nonmonotonic to monotonic with increasing applied field. In the fc profiles

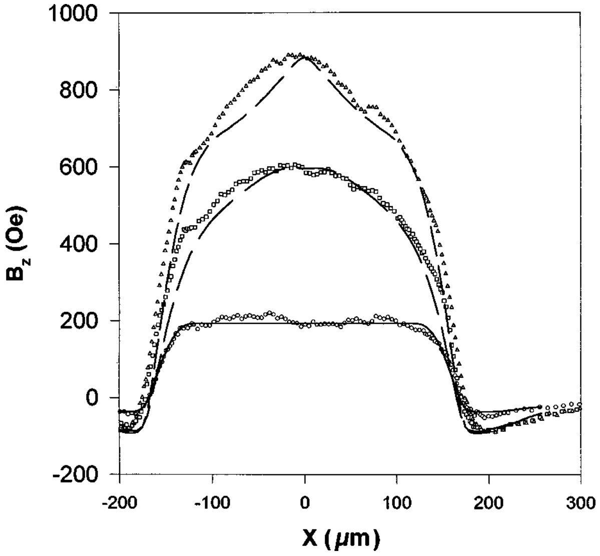

FIG. 10. Measured and fitted profiles of $B_n(x)$ in domain 2 in the field-cooled case. Shown are results for cooling to 15 K in applied fields of 200, 600, and 1000 Oe.

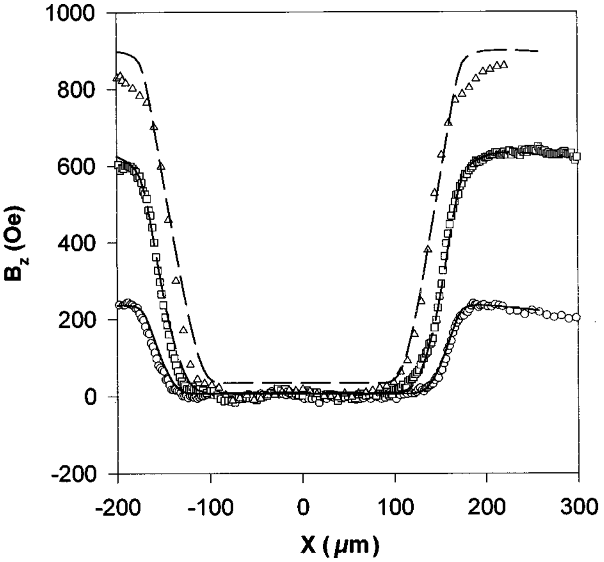

FIG. 11. Measured and fitted profiles of $B_n(x)$ in domain 2 in the zero-field-cooled case.

the wings are always nonmonotonous in cooling fields up to 1 kOe. In this case the currents near the edges are maximum because the local field in these regions (after switching off H_a) is small, and this gives rise to the observed wing shape. The suggestion that the change of the zfc wing shape is due to the field suppression of currents is consistent with the discussed model. If the effect would be dominated by a shift of the penetration front a similar wing behavior should be expected also in the fc case.

Figure 10 shows a comparison of measured trapped flux $B_n(x)$ after fc with calculated profiles for a bar containing currents which decrease towards the interior. To simplify the calculations the continuous decrease of the current corresponding to $J_c(H)$ was discretized by having two zones where the outer carries the larger $J_c^{(1)}$ and the inner the smaller $J_c^{(2)}$. The geometry is shown in the inset, and fitting parameters are given in the figure caption. Figure 11 shows similar calculations for the zfc profile with a smaller J_c in the outer ellipse. The correspondence of calculated and measured curves appears quite reasonable and supports the suggested physical picture.

TEMPERATURE DEPENDENCE AND ANISOTROPY OF CRITICAL CURRENTS

The values of the critical currents were obtained by fitting measured profiles of $B_n(x)$ across the samples in different domains. At low temperatures, when the available fields were not sufficiently large for a total penetration ($T<20$ K in domain 1 and <50 K in domain 2), the front of the magnetization was modeled by the sixth-order ellipsoid. Both J_c and the axis of the ellipsoid normal to the field were used as fitting parameters. Also a field suppression of J_c near the sample edges was accounted for in the calculations by introducing a larger ellipsoid outside where the critical current had a smaller value. This was necessary in order to reproduce the observed wing shapes of the profiles. At higher temperatures, where the penetration was complete, the measured profiles had the triangular shape and were treated as $B_n(x)$ near the top face of an infinite bar with opposite directed J_c in two halves.

Profiles of the trapped flux measured after field cooling and switching off the field were also fitted by the model of two enclosed ellipsoids, except now with the larger J_c in the outer shell. In this case the critical current is suppressed by the large field trapped in the interior part. Measured profiles having a distinct triangular shape were fitted by assuming a critical state in the whole sample. The fitting values of the larger critical current $J_c^{(1)}$ were practically the same for fc and zfc profiles measured along the same track. They were therefore taken as the small-field value of J_c in the appropriate domains. The results are presented in Fig. 12.

The $J_c(T)$ curves in all three domains have qualitatively the same shape. They are slightly curved upward towards

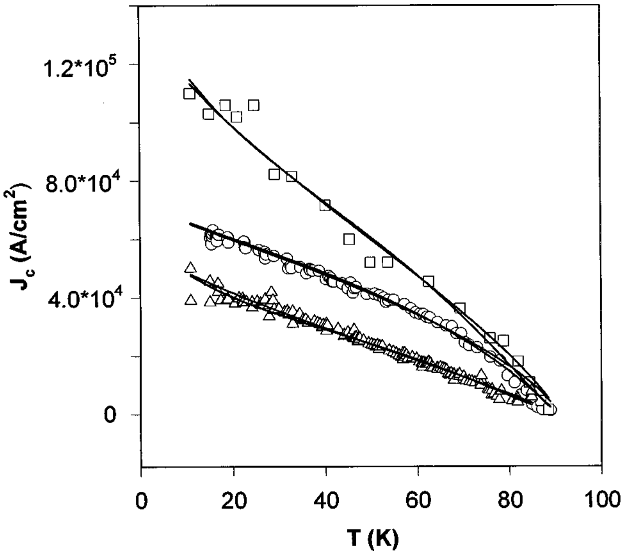

FIG. 12. Temperature dependence of J_c derived from measured flux profiles $B_n(x)$ for domains 1,2,3. Fitting of $J_c(T)$ using μ = constant and the interpolation formula $\mu=\mu(T)$ are shown.

low temperatures and drop with increasing slope near T_c. Such a behavior is commonly observed in single crystals (see, e.g., Ref. 30, and references therein) and also melt-processed samples of YBCO.[17] However, in single crystals the current decreases faster especially at intermediate temperatures, while in melted ceramics it changes more gradually and then drops sharply at $T > 80$ K. In domain 1, where the crystallite boundaries are normal to the edges and parallel to the field direction, J_c has the smallest value and drops faster with temperature than for the other domains. This current flowing across ab planes controls the flux motion along them and should be smaller as compared to J_c in domain 2, where it flows along the basal planes and resists motion of vortices at an angle to them. In domain 3, where the current flows at an angle to ab planes, and vortices also move at some angle, the J_c has an intermediate value.

The temperature dependences of the critical current in the domains were fitted by different functions in different temperature regions. First, the interpolation formula of the collective-creep model[31] was used for temperatures below 80 K,

$$J_c(T) = J_{c0}/[1 + (\mu T/U_0)\ln(t/t_{\mathrm{eff}})]^{1/\mu}. \qquad (2)$$

Here J_{c0} is the critical current in the absence of creep, U_0 is the pinning barrier at zero current, and t and t_{eff} are the characteristic experiment time and an effective attempt time, respectively. The factor $\ln(t/t_{\mathrm{eff}})$ is usually taken as a constant of the order of 30.[33,30,17] Both J_{c0} and U_0 will decrease with temperature as $[1-(T/T_c)^2]^{3/2}$ if one assumes that $J_{c0} \sim H_c/\lambda$ and $U_0 \sim H_c^2\ \xi\Delta\mathbf{d}$ with $H_c \sim 1-(T/T_c)^2$, $\lambda \sim \xi \sim [1-(T/T_c)^2]^{-1/2}$, and Δ and $\mathbf{d}$ constants.[30] The changes of the power 3/2, as was pointed out in Ref. 30, do not give an essentially different result. The exponent μ is varying from 1/7 to 3/2 and to 7/9 with decreasing current,[31] i.e., with increasing temperature. Such a variation can be modeled by a smooth function $\mu(T) = -4.16(T/T_c - 1.18)(T/T_c + 0.028)$.

The same formula for $J_c(T)$ is predicted by the vortex-glass theory,[32] which is another approach to the collective-pinning phenomenon.[33] However the exponent μ in the vortex-glass model is a constant close to unity. Both $\mu = \mathrm{const}$ and $\mu = \mu(T)$ were used in the fits shown in Fig. 12. One sees that both models can reproduce the measured curves reasonably well in a wide temperature range. For each domain, the values obtained for J_{c0} and U_0 show little dependence upon the choice of model. The result of the curve fitting, where we used $\ln(t/t_{\mathrm{eff}}) = 28$, $n = 0.5$ are as follows: In domain 1, with J_c along the c axis; $J_{c0} = 6.0 \times 10^4$ A/cm^2, $U_0 = 1250$ K for $\mu = \mu(T)$, and; $J_{c0} = 5.7 \times 10^4$ A/cm^2, $U_0 = 1700$ K for $\mu = 1$. In domain 2, with the current in the ab plane; $J_{c0} = 1.4 \times 10^5$ A/cm^2, $U_0 = 1500$ K for $\mu = \mu(T)$, and $J_{c0} = 1.35 \times 10^5$ A/cm^2, $U_0 = 1600$ K for $\mu = 1.5$. For domain 3, where J_c is at an angle with respect to the basal plane J_{c0} has an intermediate value but the pinning potential is noticeably larger; $J_{c0} = 7.2 \times 10^4$ A/cm^2, $U_0 = 3500$ K for $\mu = \mu(T)$, and; $J_{c0} = 7.2 \times 10^4$ A/cm^2, $U_0 = 3000$ K for $\mu = 2$ (this value of μ which exceeds the theoretical limit was also used by other authors, see Ref. 33).

For single crystals of YBCO a fitting of $J_c(T)$ using the interpolation formula with constant μ from 1 to 1.6 and $\ln(t/t_{\mathrm{eff}})$ from 22 to 33 gave in Ref. 30 a larger J_{c0} and a smaller U_0, both differing by an order of magnitude relative to our values. An even smaller pinning potential, <25 K, and J_{c0} increasing from 7×10^5 to 2.5×10^6 A/cm^2 with decreasing diameters of 211 particles (from 2 to 0.5 μm) were obtained in melted YBCO.[17] However in Ref. 30, J_c was measured in the field of 1 T ($H \| \mathbf{c}$), and in Ref. 17 the experiments were carried out after cooling the samples in 5.5 T. This probably explains the larger pinning potential in our case because U_0 should decrease with H. Actually, the presently found values of U_0 do not exceed the range of pinning potentials reported for YBCO crystals, e.g., 0.1–0.6 eV or 1160–6960 K in Ref. 35, and for ceramics, 0.15 eV or 1700 K in Ref. 36. For pinning to occur on an extended defect with dimension $\mathbf{d}$ the appropriate potential $(H_c^2/8\pi)\xi\Delta\mathbf{d}$ (with $\lambda = \lambda_L/\sqrt{2} = 10^3$ Å, $\xi = \sqrt{0.54}\xi_{\mathrm{BCS}} = 12$ Å,[37] and $\Delta \sim \xi$) will have a value of ~ 0.15 eV for $\mathbf{d} \sim 65$ Å. This size is quite close to the diameter of the smaller 211 particles observed in melt-processed samples using an electron microscope.[2] On the other hand, this dimension may also correspond to the length of vortex segments pinned at faces of larger particles or at other two-dimensional defects like stacking faults around 211 inclusions, grain and twin boundaries, as well as cracks.

It should be noted that the $J_c(T)$ dependences measured in Ref. 30 for YBCO crystals were fitted by the interpolation formula only up to ~ 50 K in the semilogarithmic plot, which tends to hide deviations. In Ref. 17 this fit for $J_c(T)$ in melted YBCO was used only below 35 K, whereas for the larger temperatures up to ~ 80 K the data were described by the expression for linear correlated disorder:[34] $J_c(T) = J_{c0}\exp[-3(T/T^*)^2]$ with $J_{c0} \sim (1-6) \times 10^5$ A/cm^2 and $T^* \sim 88-96$ K.

Our data can be fitted in the entire range from 15 to 80 K by the single formula (2). However, the large values found for U_0 suggest that the weak short-range disorder, due to some pointlike defects, considered in the collective-creep theory and resulting in the interpolation formula, is not the only pinning source in melt-processed YBCO. Therefore, we tested also other model descriptions of our data. The exponential dependence $J_c \sim \exp[-T/T_0]$, commonly used for HTSC's, was found to fit the data only at temperatures <60 K. The approximate relation, $J_c(T) \sim (1 - T/T_c)^{\delta}$ with $\delta \sim 1$ (actual values of δ for different domains are given in Fig. 13) could be used in a wider temperature range. However, some deviation from linearity of the log-log plot of the measured $J_c(T)$ versus $(1 - T/T_c)$ is seen, especially for the data obtained for domains 2 and 3. A striking feature of Fig. 13 is the abrupt change of the slope from $\delta \sim 1$ to $\delta \sim 1.7$ at temperatures near 80 K for domain 2 and from $\delta \sim 0.7$ to $\delta \sim 1.8$ for domain 3. Such a behavior indicates a sharp change in the vortex dynamics. One possible reason could be a transition from elastic flux creep to a plastic motion. This should occur due to the increase of U_0 with decreasing J_c assumed in the collective-creep theory.[37] In fact, in the case of plastic TAFF (thermoactivated flux flow) the pinning potential due to formation of dislocations in the flux lattice behaves as $U_0 \sim (1 - T/T_c)$,[38] and if one assumes it has a range of $\lambda \sim (1 - T/T_c)^{-1/2}$ (at higher T) one expects $J_c \sim (1 - T/T_c)^{1.5}$. Another option is a weak-link behavior of the

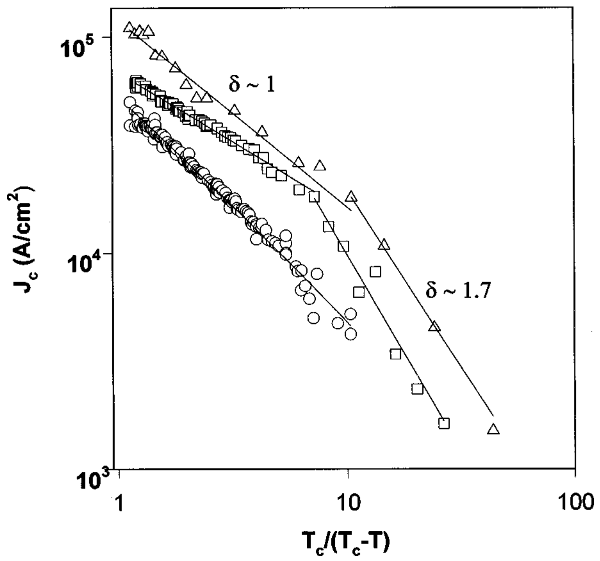

FIG. 13. Log-log plot of J_c versus $(1-T/T_c)$ for all three domains.

crystallite boundaries in domains. At lower temperatures they are frozen away, and form good contacts between the grains, whereas at higher T they can decouple and limit the current value. The theory gives $J_c \sim (1-T/T_c)^2$ for the weak-link current near T_c.[39] This is close to the dependence $(1-T/T_c)^{1.8}$ fitting our data above 80 K, and could suggest a superconductor–normal-metal–superconductor (SNS) nature of the junctions determining $J_c(T)$.[9] However, as indicated in Ref. 39, in HTSC at high temperature superconductor-insulator-superconductor junctions should show a T dependence of J_c close to that in SNS.

The weak-link scenario described above is supported also by the temperature variation in the anisotropy of J_c measured in different domains. Figure 14 shows the ratio κ of critical currents in domains 2 and 1, where the flow is along and across the basal planes, respectively. From low T and up to ~60 K the anisotropy ratio is ~2.5. This value is smaller than $\kappa = 25$ reported for MP YBCO at 5 K in Ref. 16. However, it is close to $\kappa = 3$ measured at 77 K in Refs. 15 and 29. At higher temperatures the anisotropy was found to increase sharply reaching twice the value at 80 K.

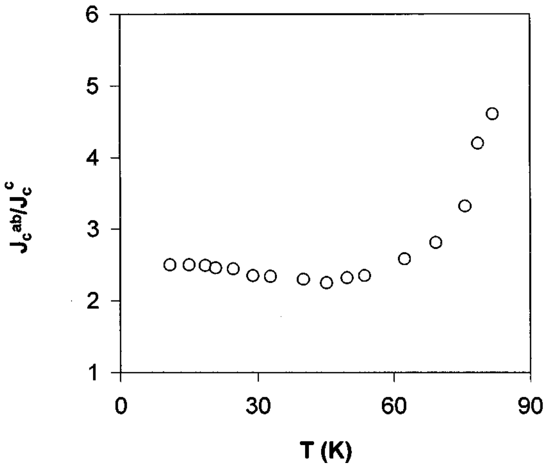

FIG. 14. Temperature variation of the current anisotropy J_c^{ab}/J_c^c obtained from $J_c(T)$ in domain 2 and domain 1.

We also note that in single crystals of YBCO the ratio J_c^{ab}/J_c^c at lower T is usually larger [in the range 5–30 (Refs. 40–43)] than the presently found value and also values obtained[15,29] for melted material. By observing the flux entry on end faces of YBCO crystals we found $\kappa \sim 14$ at temperatures from 30 to 50 K. The lower κ in melted samples seems unexpected because in this case the anisotropy should increase due to the effects of crystallite boundaries additionally decreasing the current along the c axis in domains. However, the observed results can be explained by the presence of numerous obstacles (inclusions, cracks, badly conducting parts of grain boundaries, etc.) for the current flow. This leads to wiggling current trajectories which thus pass along different crystallographic directions and result in a smearing of the effective anisotropy. Our result also differs from the behavior in 123 crystals where the anisotropy decreases with temperature.[44] The sharp increase of $\kappa(T)$ in our case, corresponding to a faster decrease of the current across aligned crystallites, could therefore indicate significant deterioration of intercrystallite contacts and formation of weak links at the boundaries for temperatures close to T_c. Additional proof for the formation of weak links on crystallite boundaries arises from magneto-optic observations of more numerous bright streaks along them during magnetization at higher T. This corresponds to decreasing currents across appropriate boundaries and easier flux entry along them. The picture is also consistent with the above discussed noticeable current suppression by the field which is known to occur in samples with weak links.

CONCLUSIONS

In the present work direct magneto-optical observations of penetration and trapping of the magnetic flux in melt-processed YBCO are carried out in a wide temperature range. The experiments reveal the behavior of such samples in bulk applications.

Similar to bicrystal boundaries in YBCO films, the boundaries between domains with different directions of the c axis show weak-link behavior at misorientation angles above ~10°. Boundaries between crystallites in domains are seen to have weaker superconducting properties at increasing temperatures and fields.

It is shown that the front of the flux penetration in superconducting rectangular bars cannot be represented by an inscribed second-order ellipsoid. Instead, an ellipsoid with sharper rounding in the corners of the samples should be used.

Due to the anisotropy of the critical current the field enters in different domains at different depths depending on the orientation of the c axis in the domain with respect to the sample edges. Appropriate values of the critical currents are extracted from profiles of induction measured across the samples in different domains using computer fitting. The temperature variation of J_c obtained in this way can be described by the interpolation formula given by the collective-creep theory, although with a large pinning energy. At temperatures above ~80 K a sharp transition to a different flux dynamics is observed. This can be associated with weak links at crystallite boundaries in domains which are frozen away, i.e., form good superconducting contacts between crystallites at lower T. Such a picture is supported by a significant increase of the anisotropy of J_c at higher T, which contrasts the behavior of 123 single crystals where the anisotropy decreases with T.

At lower temperatures the ratio of currents flowing along and across basal planes in melt-processed samples turns out to be smaller than in single crystals of YBCO. This can be explained by the wiggling of current trajectories in melted samples so that a current path in any direction contains both c- and ab-oriented segments.

ACKNOWLEDGMENTS

The Russian authors acknowledge the International Science Foundation (Grants No. RF1000 and RF1300) and the Russian Superconducting Committee (Grant No. 93211 ''Potok'') for the support. T.H.J. is grateful for the financial support of the Norwegian Research Council (NFR).

---

[1] S. Jin *et al.*, Appl. Phys. Lett. **52**, 2074 (1988).
[2] M. Murakami, *Melt Processed High-Temperature Superconductors* (World Scientific, Singapore, 1992).
[3] M. Murakami *et al.*, Supercond. Sci. Technol. **4**, S43 (1991).
[4] M. Murakami *et al.*, Physica C **185-189**, 321 (1991).
[5] S. Jin *et al.*, Appl. Phys. Lett. **54**, 584 (1989).
[6] M. Ulrich *et al.*, Appl. Phys. Lett. **63**, 406 (1993).
[7] A. Zanota *et al.*, Appl. Phys. Lett. **62**, 2722 (1993).
[8] A. Goyal *et al.*, Physica C **210**, 197 (1993).
[9] E. Z. Meilikhov, Usp. Fiz. Nauk **163**, 27 (1993); Phys. Usp. **36**, 129 (1993).
[10] D. Dimos *et al.*, Phys. Rev. B **41**, 4038 (1990); J. Mannhart *et al.*, J. Supercond. **3**, 281 (1990).
[11] A. Polyanskii *et al.*, Phys. Rev. B **53**, 8687 (1996).
[12] S. E. Babcock *et al.*, Nature (London) **347**, 167 (1990).
[13] D. Larbalestier, Phys. Today **44**(6), 74 (1991); D. Larbalestier *et al.*, Physica C **185-189**, 315 (1991).
[14] M. Turchinskaya *et al.*, Physica C **221**, 62 (1994).
[15] S. Gotoh *et al.*, Jpn. J. Appl. Phys., Part 2 **29**, L1083 (1990); Physica C **176**, 300 (1991); Supercond. Sci. Technol. **1S**, S226 (1991).
[16] Th. Schuster *et al.*, J. Appl. Phys. **74**, 3307 (1993).
[17] B. Martinez *et al.*, Phys. Rev. B **53**, 2797 (1996).
[18] K. B. Alexander *et al.*, Phys. Rev. B **45**, 5622 (1992).
[19] F. Sandiumenge *et al.*, Phys. Rev. B **50**, 7032 (1994).
[20] V. K. Vlasko-Vlasov *et al.*, Physica C **222**, 367 (1994).
[21] Z. L. Wang *et al.*, Phys. Rev. B **48**, 9726 (1993).
[22] Y. Zhu *et al.*, Philos. Mag. A **67**, 11 (1993).
[23] V. K. Vlasko-Vlasov *et al.*, Fiz. Nizk. Temp. **17**, 1410 (1991); L. A. Dorosinskii *et al.*, Physica C **203**, 149 (1992).
[24] V. K. Vlasko-Vlasov, U. Welp, G. Crabtree, D. Gunter, V. V. Kabanov, and V. I. Nikitenko, Phys. Rev. B **56**, 5622 (1997).
[25] V. K. Vlasko-Vlasov *et al.*, Physica C **222**, 361 (1994).
[26] V. K. Vlasko-Vlasov, V. V. Kabanov, V. Nikitenko, U. Welp, and G. Crabtree, JETP Lett. **65**, 264 (1997).
[27] M. A.-K. Mohamed *et al.*, Cryogenics **33**, 247 (1993).
[28] E. H. Brandt, Phys. Rev. Lett. **76**, 4030 (1996).
[29] H. C. Fan *et al.*, Physica C **185-189**, 2331 (1991).
[30] J. R. Thompson *et al.*, Phys. Rev. B **47**, 14 440 (1993).
[31] M. V. Feigelman *et al.*, Phys. Rev. Lett. **63**, 2303 (1989); M. V. Feigelman and V. M. Vinokur, Phys. Rev. B **41**, 8986 (1990).
[32] M. P. A. Fisher, Phys. Rev. Lett. **62**, 1415 (1989); D. S. Fisher *et al.*, Phys. Rev. B **43**, 130 (1991).
[33] A. P. Malozemoff, Physica C **185-189**, 264 (1991).
[34] D. R. Nelson and V. M. Vinokur, Phys. Rev. Lett. **68**, 2398 (1992); Phys. Rev. B **48**, 13 060 (1993).
[35] Y. Yeshurun and A. P. Malozemoff, Phys. Rev. Lett. **60**, 2202 (1988).
[36] H. S. Lessure *et al.*, Phys. Rev. B **40**, 5165 (1989).
[37] G. Blatter *et al.*, Rev. Mod. Phys. **66**, 1125 (1994).
[38] V. B. Geshkenbein *et al.*, Physica C **162-164**, 239 (1989).
[39] G. Deutscher and K. A. Muller, Phys. Rev. Lett. **59**, 1745 (1987).
[40] J. L. Tholence *et al.*, in *Studies of High Temperature Superconductors*, edited by A. Narlikar (Nova Science, New York, 1990), Vol. 6, p. 37.
[41] D. E. Farell *et al.*, Phys. Rev. B **36**, 4025 (1987); Phys. Rev. Lett. **64**, 1573 (1990).
[42] M. Gyorgy *et al.*, Appl. Phys. Lett. **55**, 283 (1989).
[43] K. Schonmann *et al.*, Physica C **184**, 41 (1989).
[44] J. V. Thomas, G. K. Perkins, D. E. Lacey, J. T. Totty, L. F. Cohen, A. D. Caplin, and V. I. Voronkova, in *Proceedings of the 8th International Workshop on Critical Currents in Superconductors*, edited by Teruo Matsushita and Kaoru Yamatuji (World Scientific, Singapore, 1996).